Bulletin of Geophysics and Oceanography Vol. XX, n. X, pp. XXX-XXX; Xxxxx 20xx
DOI 10.4430/bgo00501

The optimisation processing of cross-correlation calculation and dispersion measurement

G.H. Pang[1], B.X. Chen[1], P. Xue[1], Z.H. Li[2] and N.N. Zhang[1]

[1] *College of Electrical and Electronic Engineering, Changchun University of Technology, Changchun, China*
[2] *College of Automotive Engineering, Jilin University, Changchun, China*

(Received: 3 July 2024; accepted: 2 August 2025; published online: 15 April 2026)

ABSTRACT Ambient noise cross-correlation has been successfully carried out in many cases by utilising seismic data with vertical and transverse components from broadband seismographs, while both the processing of data or discussion about correlation of different components has been less demonstrated. This study concentrated on the juncture area of the Anhui, Jiangxi, and Zhejiang provinces of China, from where seismic data, between October 2014 and August 2015, were acquired through 10 domestic seismographs. Empirical Green's functions were yielded from vertical correlations or the superposition of radial and vertical correlations for the Rayleigh waves and from transverse correlations the Love waves. Then, the group-velocity and phase-velocity dispersion curves for Rayleigh and Love waves were measured by applying a frequency-time analysis method. Finally, a one-dimensional S-wave velocity structure was obtained through the joint inversion of the above dispersion measurements. The conclusions out of data processing were drawn as follows. i) The superposition of vertical and radial correlations presented the interference phenomenon: when the differences between the ratio of vertical-correlation signal-to-noise ratios (*SNR*s) to radial-correlation *SNR*s and value 1 are less than, or equal to, 0.35, the *SNR*s of the stacked vertical and radial correlations are higher. ii) The effective length of some dispersion measurements from the stacked vertical and radial correlations is longer by 2-8 s than those from the vertical correlations.

Key words: ambient noise, vertical correlation, radial correlation, dispersion measurement.

1. Introduction

The seismic data demanded for the cross-correlation of far-field ambient noise are all taken from a system comprising seismic instruments, such as broadband seismometers and broadband data loggers which are collectively called broadband seismographs. Among seismic networks in many countries, data logger series like Reftek 72, 125, and 130, as well as Quanterra Q730 and Q330, are widely deployed. Boasting high precision, wide frequency range, and an extensive dynamic range, the self-developed geophysical exploration instrument (GEI) adopted in this article is a collection and observing system for seismic signals with three components and exhibits advantages like low noise, light weight, simple connection scheme, convenient power supply, low consumption, and high stability. It can be deployed for the acquisition of broadband seismic signals especially in cases relating to long timespans of observation.

It is known that information about crustal composition can be obtained by using ambient noise data. The cross-correlation based on ambient noise is a way of utilising continuous data

from broadband recorders. The velocity structure beneath the Earth's surface can be gained through the empirical Green's function (EGF) of surface waves taken out of the cross-correlation of continuous ambient noise (e.g. Shapiro and Campillo, 2004; Sabra *et al.*, 2005; Shapiro *et al.*, 2005; Yao *et al.*, 2006; Movaghari *et al.*, 2021, Nayak *et al.*, 2021). The station pair with two three-component noise data can yield multi-component cross-correlations which have been studied and widely applied. This method is utilised to identify higher mode Rayleigh waves and improve dispersion measurements (Nayak and Thurber, 2020), to extract multimode dispersion measurements (Takagi and Nishida, 2022; Hu *et al.*, 2020), and to retrieve the observations of multiple leaking mode dispersion (Li *et al.*, 2021). In this way, earthquake signals are not required. More merits are also listed as follows: less limitation over the seismic sources and research areas, no demand on the time and spots of earthquakes, evener lateral resolution and shallower depths for obtaining velocity structures when compared with body wave tomography. In addition, integrated information of sampling medium in different irregular paths between stations can be generated with this method. Compared to direct wave, it is more sensitive to the change of medium properties. On top of this, the location of the source station can be precisely gauged thanks to it being fixed. This also leads to an unparalleled cost advantage.

Rayleigh waves are a type of seismic waves that travel along the Earth's surface in a vertical plane. They make a retrograde elliptical motion along the propagation direction. As one of the main energy sources in earthquake events, Rayleigh waves cause a major vertical displacement on the crust and surface of the Earth. Love waves are a type of seismic wave that propagates in the form of transverse wave on the surface of the Earth. They make horizontal movement, and cause the crust to vibrate from side to side, perpendicularly to the propagation direction of the wave, with almost no displacement in the vertical direction. Love waves propagate through shear deformation within the interior of the Earth and move faster when compared to Rayleigh waves. Due to an uneven density distribution of the underground structure, surface and underground medium are considered as layered medium. In addition, the velocity of the surface wave during propagation is not only related to the physical properties of the layered medium, but also to the frequency of the surface wave. That is, the surface waves present dispersion phenomena during propagation, and their dispersion characteristics lead to different arrival times and penetration depths. The surface wave velocity curve, changing with frequency, is called the dispersion curve. Therefore, if the dispersion curve of a surface wave is known, the physical properties of the underground medium can be obtained through the characteristics of the dispersion curve.

Many geophysical explorations have been carried out on the crustal structure and tectonic deformation process of southern China, including active source seismic detection (Xiong *et al.*, 2009), receiver function (Zhang *et al.*, 2018), body wave tomography (He and Santosh, 2016), and surface wave tomography (Lü *et al.*,2016; Gao *et al.*, 2022). These are studies on large-scale crustal structures of southern China, while this study focuses on the crustal velocity structure between two separate positions in a determined area of southern China. This study first introduces the research data and their preprocessing. Next, it describes the computation of cross-correlation functions and the extraction of dispersion curves. Finally, these dispersion data are utilized to invert the one-dimensional (1D) crustal velocity structure near the junction of the three southern provinces.

2. Data and preprocessing

For this experiment, a total of 10 seismic stations were deployed in a longitude from 115.2° E to 119.7° E and latitude from 28° N to 30.2° N by Jilin University. With CMG-3ESPC (a three-component broadband seismometer with output signal frequency between 60 and 50 Hz) for C2, C3, C6, C14, C40, C39, C42, C50, C45, and CMG-3T (120 s -50 Hz) for C37, the 10 stations were all equipped with GEI and kept recording consecutive seismic data from October 2014 to August 2015. Their distribution is illustrated in Fig. 1.

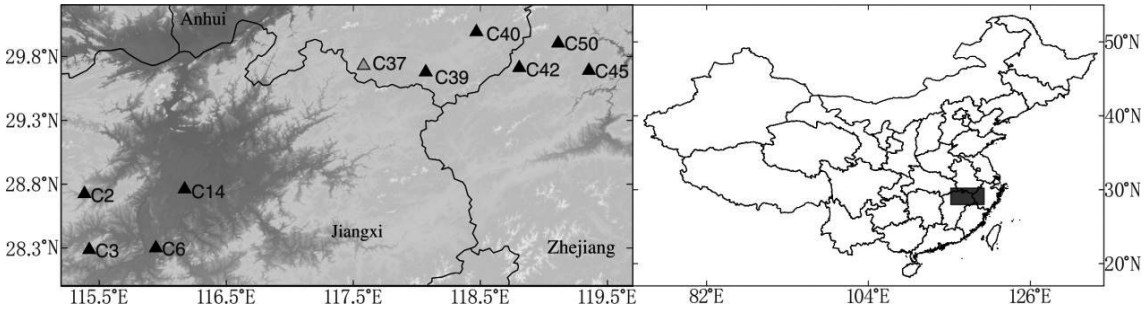

Fig. 1 - The distribution of 10 stations and the background tectonic map of the study area. The triangles indicate the broadband stations (left). The position of the study area in China (right).

The processing scheme (Table 1) stemmed from Bensen *et al.* (2007). Firstly, the east (E), north (N), and vertical (Z) component data of 24-hour continuous passive records were preprocessed, prior to cross-correlation, by decreasing their sampling frequency to 1 Hz. Then, detrend and the removal of average and instrumental response from 24-hour continuous time series were operated. Next, the seismic data were band-pass filtered at a frequency range of 2.25 to 60 s. Then, the influence of unusual signals and other irregularities were debilitated by performing normalisation in time domain. Lastly, spectrum whitening was applied to dodge sizable imbalance in spectrum and raise the bandwidth of ambient noise.

Table 1 - Preprocessing steps.

1	Decreasing sampling frequency.
2	Removing the average and detrend.
3	Removing the instrumental response.
4	Band-pass filtering.
5	Time-domain normalisation.
6	Spectrum whitening.

3. The cross-correlation calculation

The data from the broadband stations contain E, N, and Z components. Fig. 2 shows that E1, N1, and Z1, and E2, N2, and Z2 refer to the data components of station 1 and station 2, respectively.

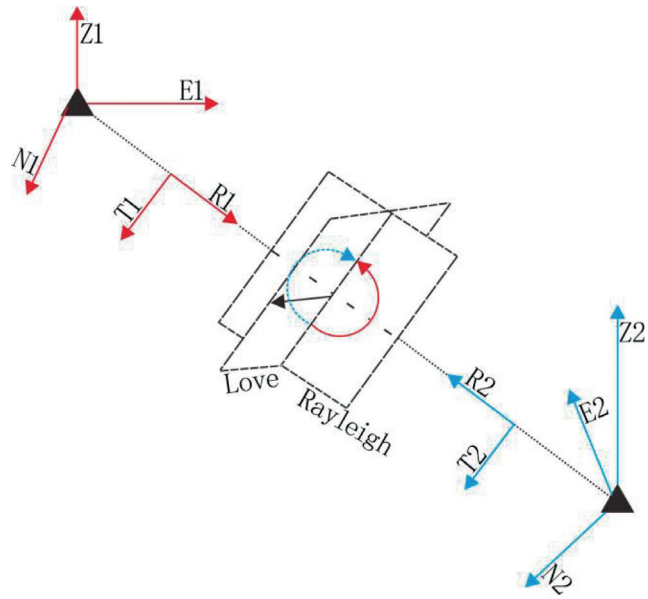

Fig. 2 - The diagram of Z, N, E, R, and T directions. The black triangles indicate the broadband stations.

R1 and R2 and T1 and T2 stand for the radial components and transverse components between two stations, respectively. T1 is perpendicular to R1, and T2 is perpendicular to R2. Moreover, it can be concluded from Fig. 2 that the Rayleigh waves were from Z-Z or R-R cross-correlations; Love waves were from T-T cross-correlations.

Table 2 - The processing steps for the cross-correlation.

1	Cutting data by two hours.
2	Calculating Z-Z cross-correlations for every hour.
3	Stacking all above Z-Z cross-correlations.
4	Stacking positive and negative cross-correlations.
5	Repeating steps 2 to 4, but for E-E, E-N, N-E, and N-N components.
6	Rotating E-E, E-N, N-E, and N-N cross-correlations into T-T, R-R, T-R, and R-T cross-correlations.

The preprocessed data with three components from each station were cut into two-hour data sections (Table 2). Then, the component cross-correlations (E-E, E-N, N-E, N-N, and Z-Z) of two-hour sections between each station pair were calculated, and all the two-hour cross-correlations from October 2014 to August 2015 were stacked to obtain an asymmetric cross-correlation waveform. A re-stacking between the positive and negative sides of the waveform followed to gain a symmetric shape, by which the signal-to-noise ratios (*SNR*s) were improved. Fig. 3 served as an example of the symmetric cross-correlations from station pair C2-C40. It can be observed in Fig. 3 that the arrival time of the N-N cross-correlation signal was earlier than that of other signals. In addition, all available symmetric Z-Z cross-correlations were presented in Fig. 5a.

Using a rotation matrix (Lin *et al.*, 2008), the cross-correlations for the N–N, N–E, E–N, and E–E components were, then, rotated into T-T, R-R, T-R, and R-T components as shown in Fig. 4. Figs. 5b and 5c displayed the cross-correlations for the T-T and R-R components of all station

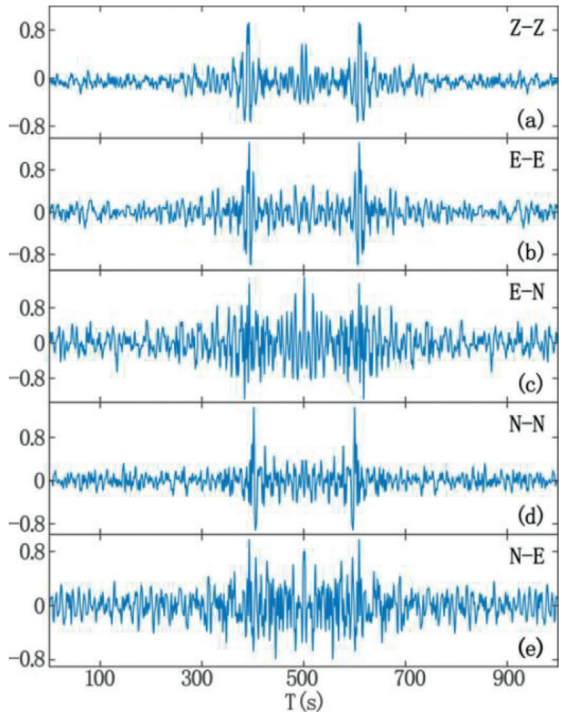

Fig. 3 - The cross-correlations of Z–Z, E–E, E–N, N-N, and N–E components between stations C2 and C40.

pairs, with the red and blue lines representing the propagation-time window of the signal with 3 km/s and 5 km/s, respectively.

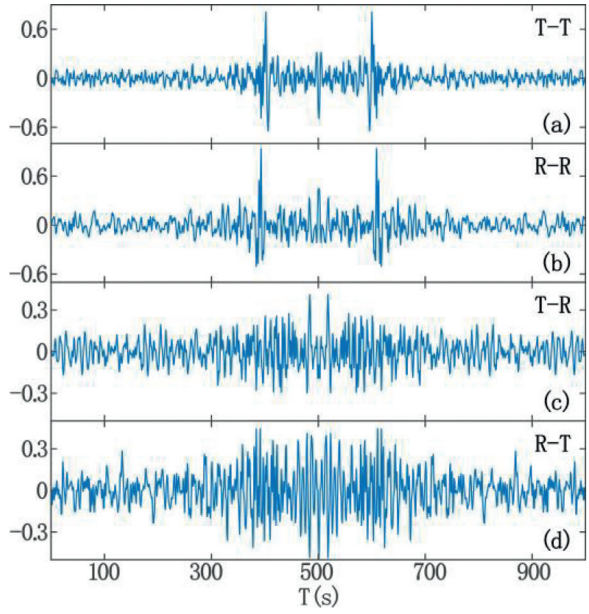

Fig. 4 - The cross-correlations of the T–T, R–R, T–R, and R-T components between stations C2 and C40.

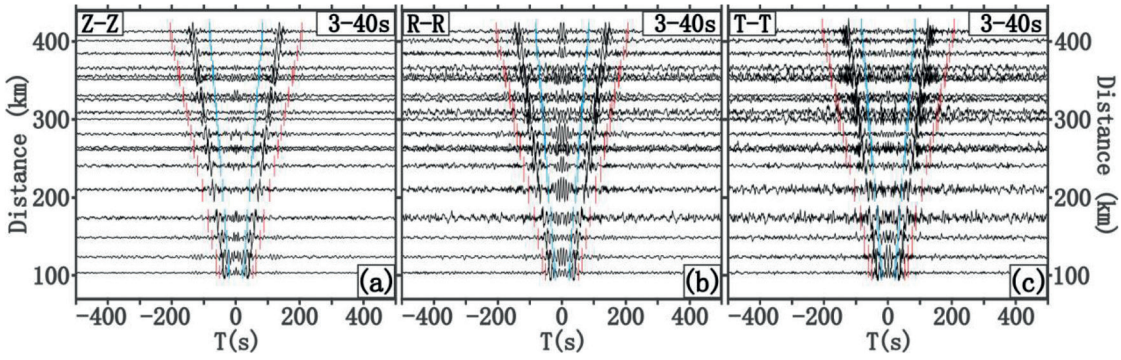

Fig. 5 - All the Z-Z, R-R, and T-T cross-correlations. The blue and red lines represent the arrival times of velocity 5 km/s and 2 km/s, respectively.

4. Rayleigh waves, Love waves, and cross-correlations of different components

4.1. Rayleigh waves and Love waves

As shown in Fig. 2, Love waves can be obtained from T-T correlations, and Rayleigh waves from Z-Z or R-R correlations. Furthermore, Rayleigh waves can also be obtained from the superposition of Z-Z and R-R correlations which are denoted as ZZ+RR correlations. The Z-Z, R-R, and ZZ+RR correlations all contain Rayleigh-wave signals, and the differences between their *SNR*s are described as follows.

4.2. The SNR*s of Rayleigh-wave Z-Z, R-R, and ZZ+RR correlations*

A correlation waveform contains surface-wave signal data and noise data. The signal window is set at 2-5 km/s (V_{min}, V_{max}) and the arrival time of the signal window is $t_1 = X/V_{max}$, $t_2 = X/V_{min}$, where X is the distance between the two stations. The 150-second records after the signal window are set as noise windows. The ratio of the maximum amplitude within the signal window to the mean square deviation within the noise window is the *SNR*, as expressed by the formula below:

$$SNR = max\,(|signal|)/std(noise). \quad (1)$$

The 19 station-pair cross-correlations in the 3-40-second period range of Z-Z, R-R, and ZZ+RR, containing obvious signals, were selected from 45 station-pair cross-correlations, and their *SNR*s are shown in Fig. 6a. It can be observed that the *SNR*s of the ZZ+RR cross-correlations are greater than those of the Z-Z and R-R cross-correlations in the dark grey background in Fig. 6a, whereas that in the light grey background in Fig. 6a is exactly the opposite. In Fig. 6a, the *SNR*(ZZ) represents the *SNR*s of the Z-Z cross-correlations, the same as *SNR*(RR) and *SNR*(RR+ZZ) but for Z-Z cross-correlations and the stacking of R-R cross-correlations and Z-Z cross-correlations, respectively. Fig. 6b is the absolute value of the difference between the ratio of the *SNR*(ZZ) to the *SNR*(RR) and value 1. Fig. 6c is the ratio of the *SNR*(RR+ZZ)-max[*SNR*(ZZ),*SNR*(RR)] to max[*SNR*(ZZ),*SNR*(RR)]. In addition, Figs. 6b and 6c imply that the higher the degree of equality between the *SNR*s of Z-Z and R-R cross-correlations, the larger the difference between the *SNR*s of ZZ+RR and Z-Z or R-R cross-correlations, which conforms to interference phenomenon.

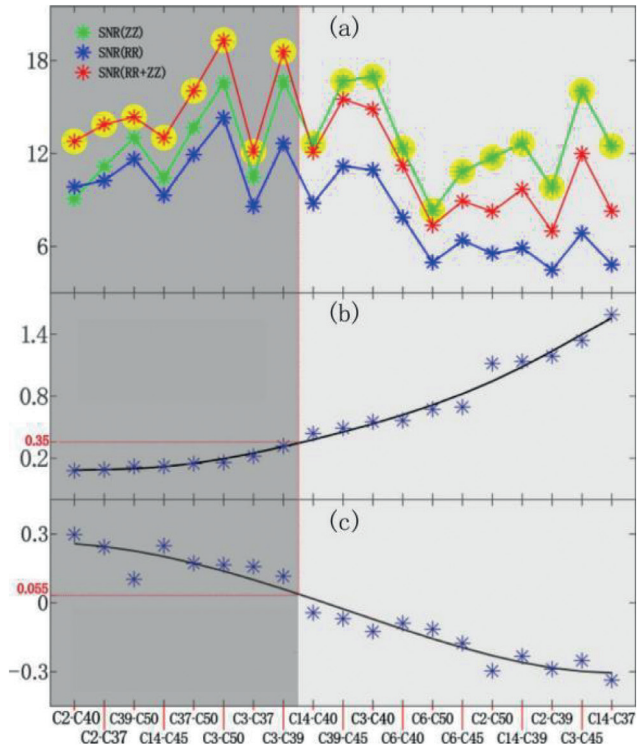

Fig. 6 - The *SNR*s of Z-Z, R-R, and ZZ+RR cross-correlations and their numerical relationship.

The interference phenomenon suggests that the waveform superposition of Z-Z and R-R cross-correlations could efficiently improve the *SNR*s of the Rayleigh waves. For example, the cross-correlations in the 3-40-second period range of station pair C3-C39 for Z-Z, R-R and ZZ+RR are expressed in Fig. 7, which intuitively displays that the signal of the ZZ+RR cross-correlations in 3-40 s was clearly stronger than that of the Z-Z or R-R cross-correlations. Additionally, the *SNR*s at periods from 3 s to 40 s of station pairs C2-C37 and C2-C39 are presented in Fig. 8. More specifically, within the *SNR*>5 scope, the *SNR*s of ZZ+RR between stations C2 and C37 are higher than those of Z-Z or R-R when the period is greater than 13.1. This, instead, is the contrary for station pair C2-C39 even throughout the entire period, with no *SNR*s of the ZZ+RR cross-correlations stronger than those of the ZZ cross-correlations or ZZ+RR cross-correlations, simultaneously.

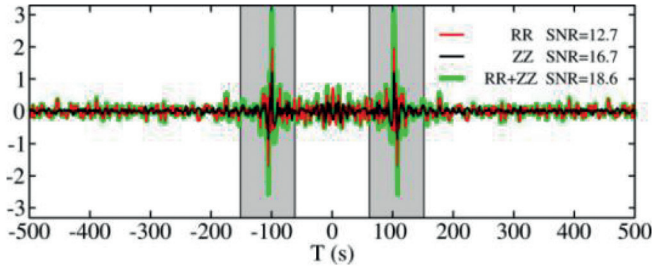

Fig. 7 - The Z-Z, R-R, and ZZ+RR cross-correlations between stations C3 and C39.

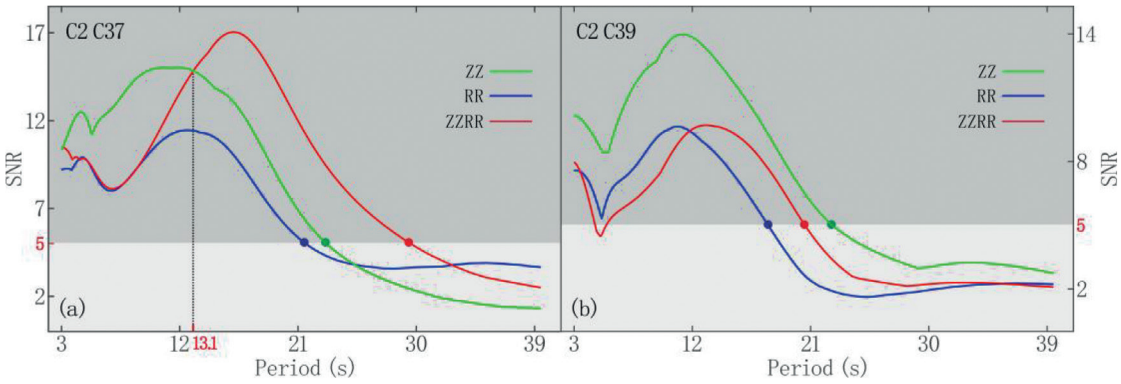

Fig. 8 - The *SNR*s of the Z-Z, R-R, and ZZ+RR cross-correlations of station pairs C2-C37 and C2-C39 at different periods.

4.3. The SNR*s of the Rayleigh-wave Z-Z correlations and their positive and negative components*

The average *SNR*s of the negative (ZZ-) and positive components (ZZ+) and their stack (ZZ+-) of Z-Z cross-correlations are detected in Fig. 9. As can be seen in Fig. 9, the average *SNR*s of ZZ- and ZZ+- decrease progressively from the periods at 3 and 40 s with sharp slipping after 11.5 s especially, and maximise at the beginning of the 3-second period, with a bottom peak at the 7-second period and a top peak at 11.5 s especially. Moreover, the two low peak shapes are quite similar, just like the two top peak shapes. The reason for this needs further analysis. Although the average *SNR*s of ZZ- are distinctly higher than those of ZZ+- after the period at 20 s, the cross-correlations of the ZZ+- gain more long-term dispersion.

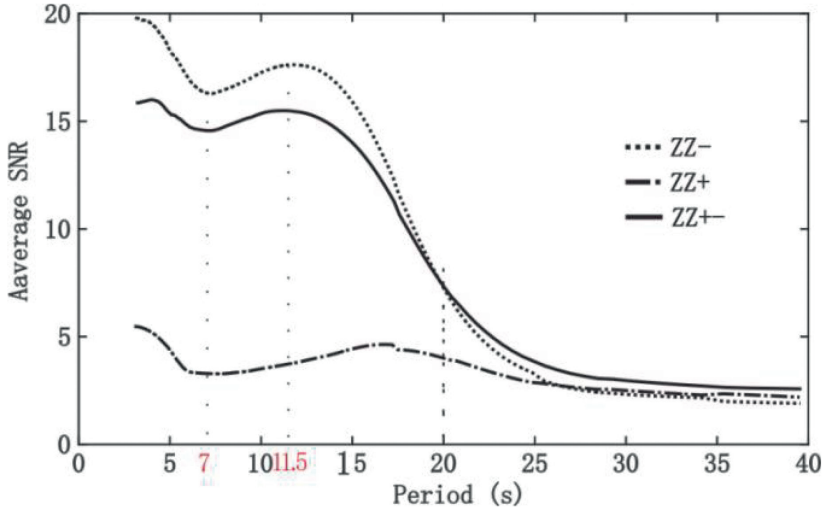

Fig. 9 - The average *SNR*s of all Z-Z cross-correlations; ZZ-, ZZ+, and ZZ+- representing the negative, positive, and their stacked component cross-correlations, respectively.

5. Group and phase velocity dispersion measurement

5.1. Group velocity dispersion measurement

The group velocity dispersions of the Rayleigh waves and Love waves were measured by applying the multiple filtering method (Dziewonski *et al.*, 1969), which can rapidly extract the entire dispersion curve. The processing steps (Fang, 2019) are shown in Fig. 10. $W_{(t)}$ *i*s the time-domain signal of the symmetric cross-correlations. More specifically, if $W_{(t)}$ is the Z-Z, R-R or ZZ+RR cross-correlation, $U(\omega)$ is the Rayleigh-wave group velocity dispersion; if $W_{(t)}$ is the T-T cross-correlation, $U(\omega)$ is the Love-wave group velocity dispersion. *r* is the distance between the station pair. In addition, $G(\omega)$ is obtained from $W(\omega)$ with the Gauss filtering function with parameter *a*, and the set of parameter *a* is as followed.

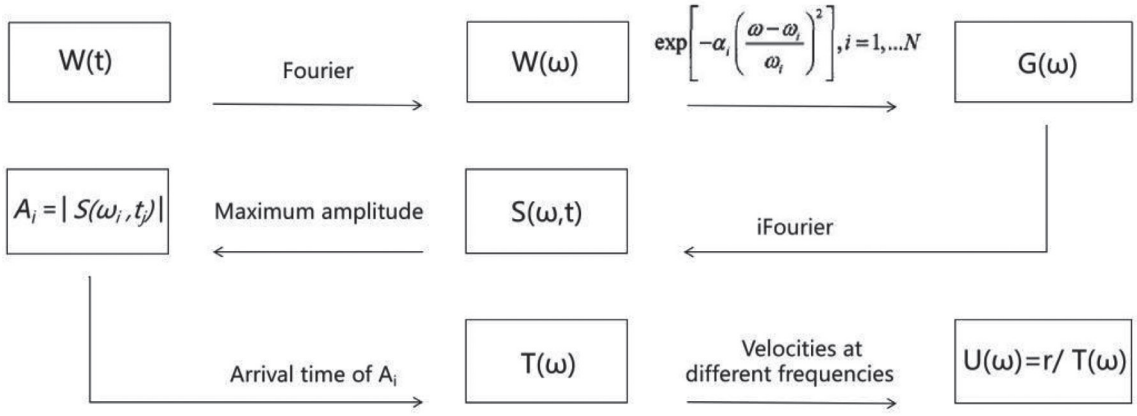

Fig. 10 - The multiple filtering method process.

1) The centre frequency, ω_i, in the Gaussian filtering function $\exp\left[-a_i\left(\frac{\omega-\omega_i}{\omega_i}\right)^2\right]$ was set at $1/3\left[\omega_i = \frac{1}{T_i},\ T_i = (3-40)s\right]$ in the first cycle;
the moving window a_i was set from 0.001 to 20 with an interval of 0.001, and the corresponding different *S(ω,t)s* was obtained.
2) The *SNR*s of all the *S(ω,t)s* obtained in step 1 were calculated, and the maximum *SNR* and its corresponding a_i (defined as the best a_i) were picked. Steps 1 and 2 were exemplified by Rayleigh-wave cross-correlations $W(\omega)$ of C39-C50. More specifically, with the a_i value set within 0.001-20, the *SNR*s of cross-correlations *S(ω,t)* filtered by the Gauss filtering at 4 s, 8 s, 12 s, and 15 s, respectively, are shown with curves in Fig. 11, in which the four curves all have a best a_i (solid dots in Fig. 11). In addition, with a_i at 1.179, 5, 10, and 15, respectively, the four waveforms of *S(ω,t)s* from $W(\omega)$, obtained with Gaussian filtering at the centre period at 4 s, are shown in Fig. 12 which exhibits gradual wave distortion and *SNR* descent (Figs. 12a to 12d). The *SNR* value 1.179 corresponds to the pink dot in Fig. 11. Fig. 13, with a long period of 16 s and a_i value at 5, 10, 15, and 20, illustrates that as the a_i value increases, its waveform amplitude of *S(ω,t)*, as well as *SNR*, decreases, while waveform shapes show no change.

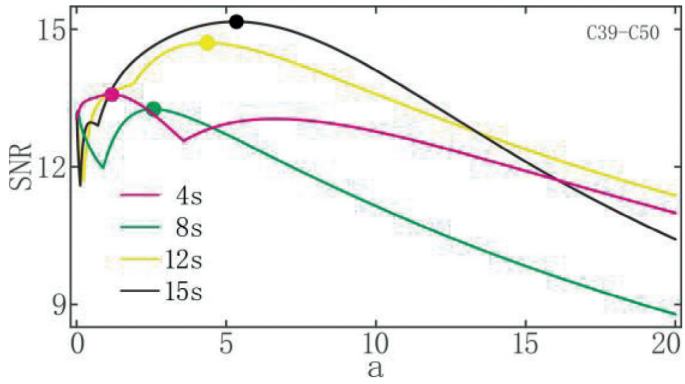

Fig. 11 - The *SNR*s of the Z-Z cross-correlations filtered with the Gauss filtering function with different a_i values.

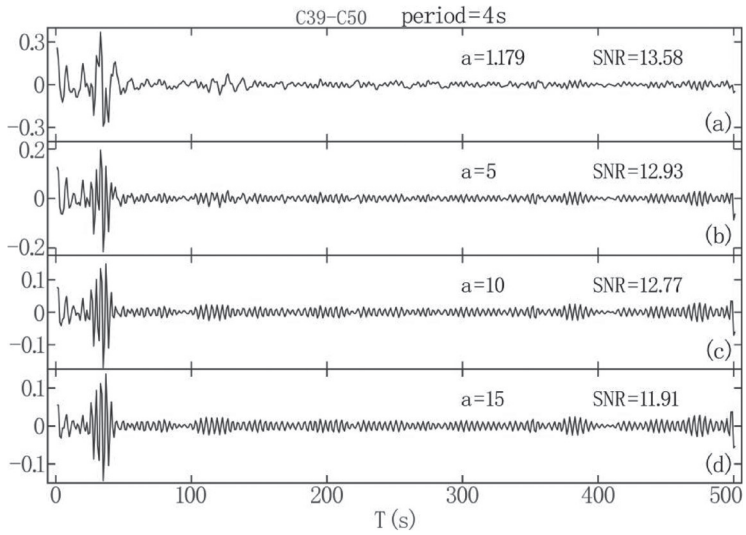

Fig. 12 - The Z-Z cross-correlations filtered with the Gauss filtering function with different a_i values and centre period at 4 s.

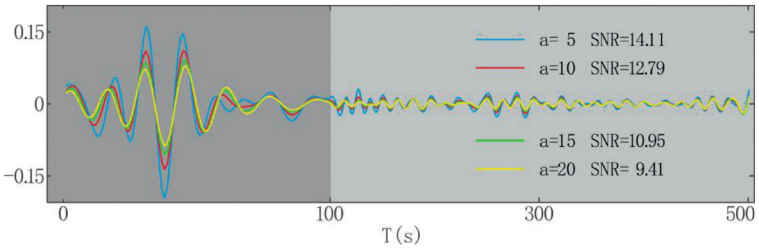

Fig. 13 - The Z-Z cross-correlations filtered with the Gauss filtering function with different a_i values and centre period at 16 s.

3) All the best a_i values in the period between 3 and 40 s were drawn up. For example, for station pair C39-C50, all its best a_i values are shown to form the blue line in Fig. 14, which ends up at period 17 s due to waveform distortion in the period between 18 and 40 s, with its four dots corresponding to the four in Fig. 11.

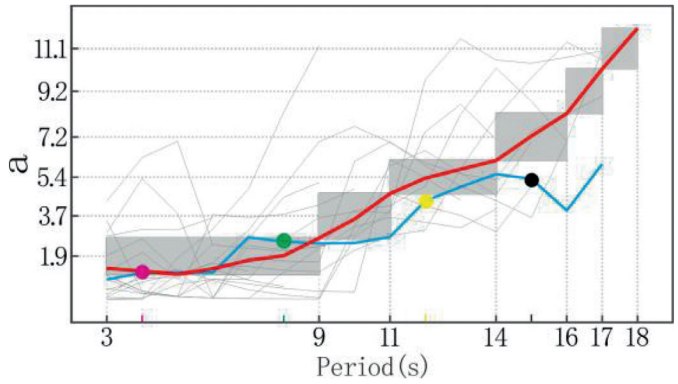

Fig. 14 - The average a_i values at different period sections.

4) Then, all selected Rayleigh cross-correlations copy steps 1, 2, and 3 to obtain their best a_i curves (i.e. the light grey curves in Fig. 14), after which the average-value curve (the red line) is acquired.
5) Based on the red line, the average a_i value at different period sections can be determined. For example, 1.9, 3.7, 5.4, 7.2, 9.2, and 11.1 at period sections of 3-9 s, 9-11 s, 11-14 s, 14-16 s, 16-17 s, and 17-18 s, respectively, and 12 at the period section of 19-40 s, due to the trend of the red curve.
6) Likewise, the Love wave duplicated the five steps above, and its average a_i value is 1.6, 3.7, 5.9, 7.7, and 9.6 at different period sections of 3-9 s, 9-11 s, 11-13 s, 13-15 s, and 15-18 s, respectively. Compared to the Rayleigh wave, the Love wave generally showed lower average a_i values.

Fig. 15b presents the Rayleigh cross-correlation waveform of C3-C50. The waveform was processed through multiple filtering methods and, then, as shown in Fig. 15c, the group-velocity dispersion curve, was acquired. Fig. 15c represents the dispersion curve, and its corresponding

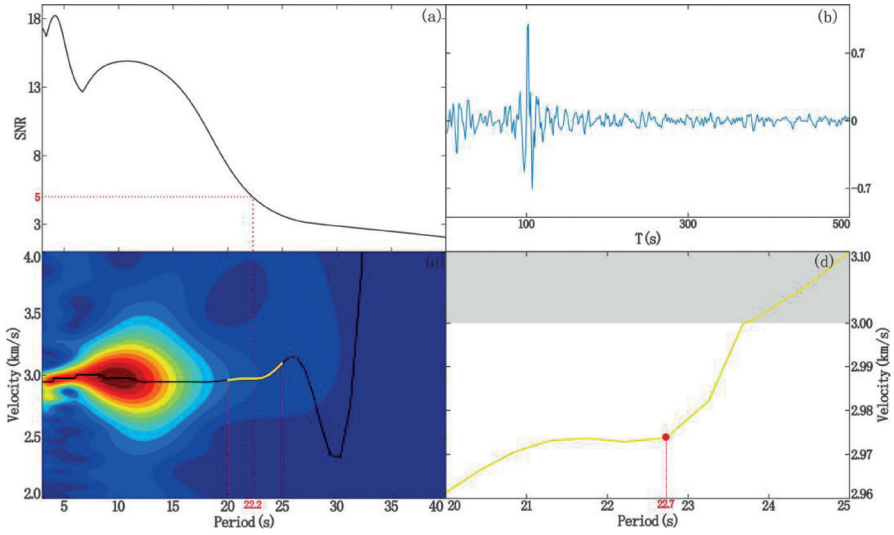

Fig. 15 - a) The *SNR* of the dispersion curve; b) the original cross-correlation; c) diagram of the Rayleigh wave group-velocity dispersion measurement for C3-C50; d) the enlarged version of the yellow section in panel c.

*SNR*s are shown in Fig. 15a. By combining Figs. 15a and 15c, it can be observed that the *SNR*s of the dispersion curve are greater than 5 within the period range of 3 s to 22.2 s. Fig. 15d displays the dispersion curve with the period range of 20 s to 25 s, where a turning point is identified at a period of 22.7 s. Based on the principle of dispersion curve continuity, the effective period range of the dispersion curve is therefore determined to be from 3 s to 22.7 s.

In addition, Fig. 16 shows the dispersion curves of ZZ, RR, and ZZ+RR cross-correlations and reports that, compared to the ZZ and RR components, the ZZ+RR component can lead to longer valid group velocity dispersion curves.

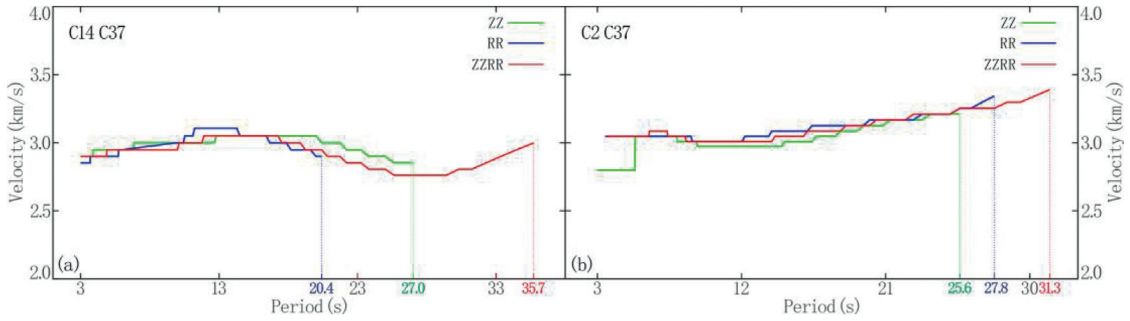

Fig. 16 - Group velocity dispersion curves of the ZZ, RR, and ZZ+RR cross-correlations based on station pairs C14-C37 (a) and C2-C37 (b).

5.2. Phase velocity dispersion measurement

The phase velocity dispersion curve of the EGF was considered by utilising an improved far-field approximation of the image transformation analysis technique by Yao *et al.* (2006). On the matrix image of cross-correlation amplitude, the entire dispersion curve can be automatically obtained. We displayed the curve from C2-C50 in Fig. 17. The red dots in Fig. 17c were automatically picked and formed the dispersion curve from the EGF at the 3-40-second period; the black, blue, and red curves in Fig. 17b represent the original cross-correlation, cross-correlation signal, and noise signal; the red dots in Fig. 17a indicate the extracted dispersion points with *SNR* values greater than 5.

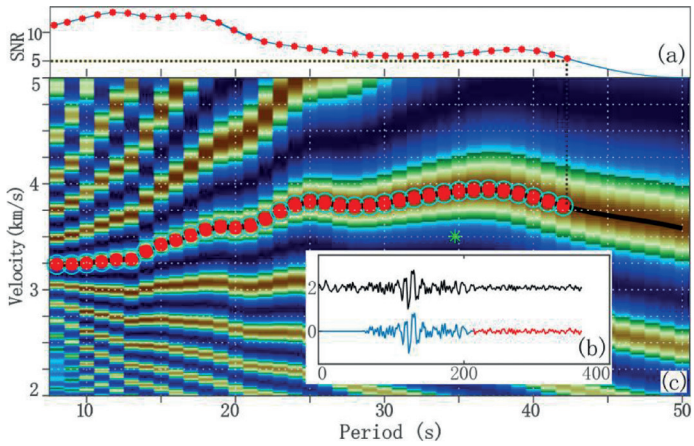

Fig. 17 - a) The *SNR* of the dispersion curve; b) the original cross-correlation; c) diagram of the Rayleigh wave phase-velocity dispersion measurement for C2-C50.

5.3. The selection of group and phase velocity dispersions

The three steps below were followed to rule out unreliable signals. Firstly, the measurements were abandoned considering not only their *SNR*s less than 5 but also the turning point. In addition, distance between two stations should be longer than two wavelengths. Measurements were discarded when $X<2\ V_{max}\times T_{max}$, with X and V_{max} representing the distance and the assumed maximum surface-wave velocity, respectively. Lastly, a cluster analysis (e.g. Ritzwoller and Levshin, 1998) and a morphological analysis were performed to remove unreasonable ones.

After following the three steps above, the valid dispersion curves for the C2-C40, C2-C50, C3-C45, and C6-C45 station pairs were acquired and displayed in Fig. 19, serving as the basis of the following inversion.

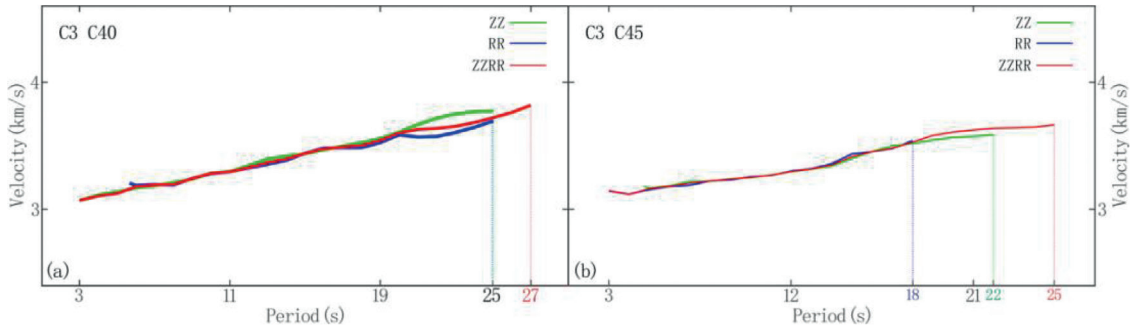

Fig. 18 - Phase velocity dispersion curves of the ZZ, RR, and ZZ+RR cross-correlations based on station pairs C3-C40 (a) and C3-C45 (b).

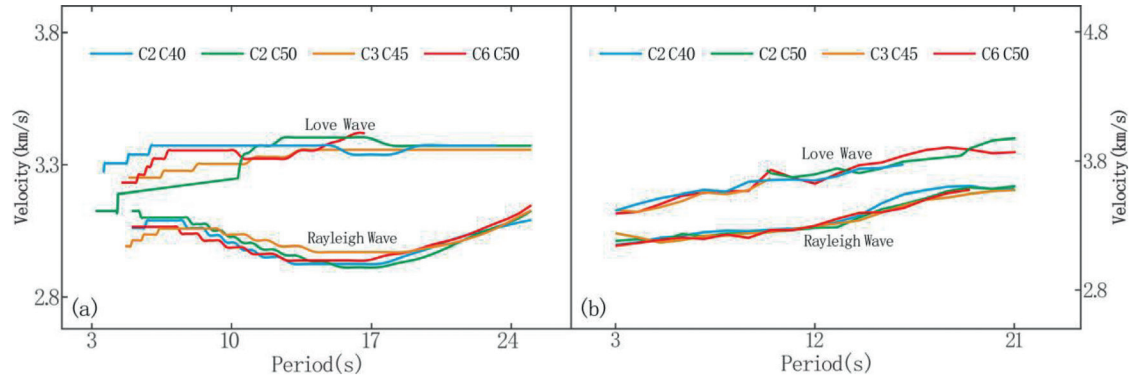

Fig. 19 - Group (left) and phase (right) dispersions for the Love wave and Rayleigh wave.

6. Inversion for shear wave-velocity structure

The dispersion curves were extracted from the Rayleigh and Love wave group and phase velocities obtained from the previous section. By simultaneously inverting the dispersion curve data, we used the programme developed by Herrmann and Ammon (2004) with linear steps to obtain the 1D shear-wave velocity (*Vs*) structure.

Due to the limited amount and short period of dispersion data involved in the inversion, the inversion results place greater focus on studying the overall velocity changes in the study area. So the initial model used was a half space model and not a gradient model as the inversion results obtained with the half space model can better reveal the overall velocity changes. The parameters of the initial model are from Crust 1.0 (Laske *et al.*, 2013), specifically, the average value of the Crust 1.0 parameters between the two stations constitute an initial model. The algorithm iteratively perturbed a layered velocity profile before achieving best similarity between recorded dispersion curves and the theoretical ones. More specifically, dispersion-curve data were brought into a model with parameters agreeing with Crust 1.0 (Laske *et al.*, 2013). The model counts 35 layers, with each one representing one kilometre, and parameters including depth, density, P-wave velocity, and S-wave velocity. They are set in the model to perform the inversion of the dispersion obtained.

The average *Vs* structure of a station pair was illustrated in this paper. The velocity-distribution patterns of station pairs C2-C40, C2-C50, and C6-C50, in Figs. 20a to 20c, shared essential similarities, with only slight variations in depth between 17 and 23 km. However, the *Vs* beneath C3-C45 in Fig. 20d, transecting only the Jiangxi province and Zhejiang province, was visually distinct from the others: among the four inversions, the *Vs* of the middle crust, with a depth of 7-18 km, was the highest with a maximum gap of 0.111km/s.

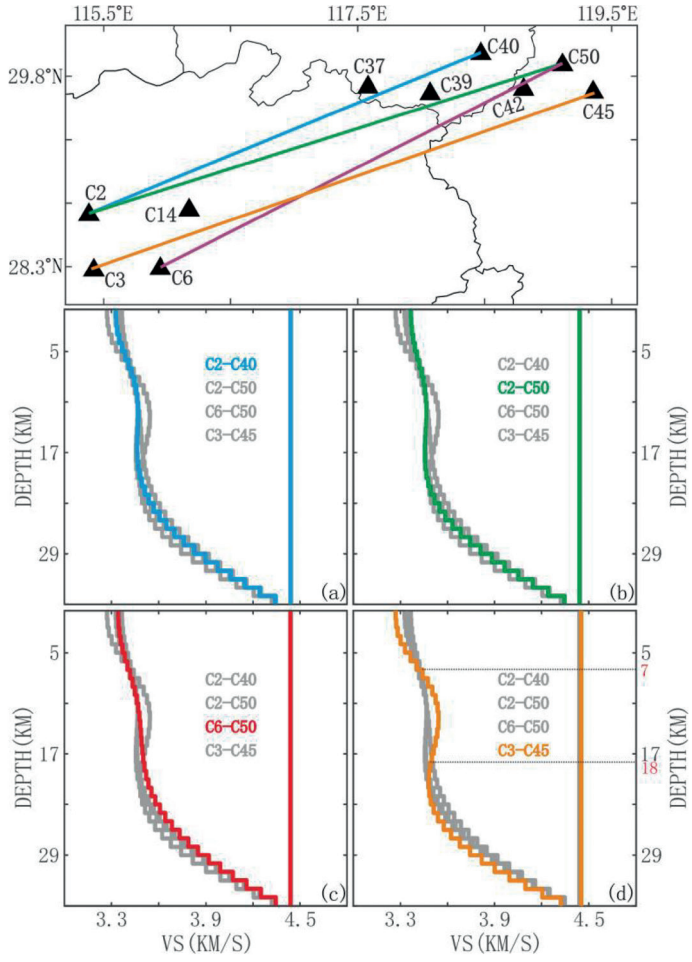

Fig. 20 - The inversion results of the *Vs* structures in the crust with a depth of 0-35 km of the four station pairs in Fig. 11.

7. Conclusions

This paper introduced that the noise cross-correlation functions were retrieved by processing time series of three-month ambient noise between station pairs observed at the 10 broad-band stations; group-velocity dispersions were measured by utilising the multiple filtering method and phase-velocity dispersions were measured by utilising the modified far-field approximation of image transformation analysis technique. Lastly, the selected Rayleigh and Love dispersion measurements were adopted to invert a 1D S-wave velocity structure with a depth of 35 km. The conclusions on the data processing process and inversion are summarised as follows: some superposition of vertical and radial correlations increased the energy of the Rayleigh wave effectively and extended the effective length of the dispersion curves. The crust, with a depth of 7-18 km beneath the junction of the Jiangxi and Zhejiang provinces, featured lower velocities, compared to the other three inversion results, with the maximum gap at 0.111 km/s.

Acknowledgments. We express our sincere thanks for the support and help provided by all the teachers and students in the seismic group of Jilin University.

REFERENCES

Bensen G.D., Ritzwoller M.H., Barmin M.P., Levshin A.L., Lin F., Moschetti M.P., Shapiro N.M. and Yang Y.; 2007: *Processing seismic ambient noise data to obtain reliable broad-band surface wave dispersion measurements*. Geophys. J. Int., 169, 1239-1260.

Dziewonski A., Bloch S. and Landisman M.; 1969: *A technique for the analysis of transient seismic signals*. Bull. Seismol. Soc. Am., 59, 427-444, doi: 10.1785/BSSA0590010427.

Gao L., Zhang H., Gao L., He C., Xin H. and Shen W.; 2022: *High-resolution Vs tomography of south China by joint inversion of body wave and surface wave data*. Tectonophys., 824, 229228, doi: 10.1016/j.tecto.2022.229228.

He C. and Santosh M.; 2016: *Crustal evolution and metallogeny in relation to mantle dynamics: a perspective from P-wave tomography of the south China block.* Lithos., 263, 3-14.

Herrmann R.B. and Ammon C.J.; 2004: *Surface waves, receiver functions and crustal structure*. Comput. Programes Seismol., Vers. 3.30, Saint Louis University, Saint Louis, MO, USA, http://www.eas.slu.edu/People/RBHerrmann/CPS330.html.

Hu S., Luo S. and Yao H.; 2020: *The Frequency-Bessel Spectrograms of multicomponent cross-correlation functions from seismic ambient noise*. J. Geophys. Res.: Solid Earth, 125, e2020JB019630, doi: 10.1029/2020JB019630.

Laske G., Masters G., Ma Z. and Pasyanos M.; 2013: *Update on CRUST 1.0: a 1-degree global model of Earth's crust*. Geophys. Res. Abstr., 15, EGU2013-2658.

Li Z., Shi C., Ren H. and Chen X.; 2022: *Multiple leaking mode dispersion observations and applications from ambient noise cross-correlation in Oklahoma*. Geophys. Res. Lett., 49, e2021GL096032, doi: 10.1029/2021GL096032.

Lin F.C., Moschetti M.P. and Ritzwoller M.H.; 2008: *Surface wave tomography of the western United States from ambient seismic noise: Rayleigh and Love wave phase velocity maps.* Geophys. J. Int., 173, 281-298, doi: 10.1111/j.1365-246X.2008.03720.x.

Liu T.T.; 2014: *Research on testing and application methods of broadband seismographys*. Master's Thesis in Geophysical Sciences, Jilin University, Changchun, Jilin, China.

Lü J., Xie Z.J., Zheng Y., Zha X.H., Hu R. and Zeng X.F.; 2016: *Rayleigh wave phase velocities of south China block and its adjacent areas*. Sci. China Earth Sci., 59, 2165-2178.

Movaghari R., JavanDoloei G., Yang Y., Tatar M. and Sadidkhouy A.; 2021: *Crustal radial anisotropy of the Iran plateau inferred from ambient noise tomography*. J. Geophys. Res.: Solid Earth, 126, e2020JB020236, doi. 10.1029/2020JB020236.

Nayak A. and Thurber C.H.; 2020: *Using multicomponent ambient noise cross-correlations to identify higher mode Rayleigh waves and improve dispersion measurements*. Geophys. J. Int., 222, 1590-1605, doi: 10.1093/gji/ggaa270.

Nayak A., Ajo-Franklin J., Cheng F., Rodriguez Tribaldos V., Dobson P., Wood T., Robertson M., Mellors R., Rotermund C., Dong B., Monga I., Popescu A., Shang Y., Maher E., Morency C., Matzel E., Metcalfe E., Morse L., Templeton D. and Wu K.; 2021: *Measurement of surface-wave phase-velocity dispersion on mixed inertial seismometer – Distributed acoustic sensing seismic noise cross-correlations*. Bull. Seismol. Soc. Am., 111, 3432-3450, doi: 10.1785/0120210028.

Ritzwoller M.H. and Levshin A.L.; 1998: *Surface wave tomography of Eurasia: group velocites*. J. Geophys. Res., 103, 4839-4878.

Sabra K.G., Gerstoft P., Roux P., Kuperman W.A. and Fehler M.C.; 2005: *Extracting time-domain Greens function estimates from ambient seismic noise*. Geophys. Res. Lett., 32, L03310, doi: 10.1029/2004GL021862.

Shapiro N.M. and Campillo M.; 2004: *Emergence of broadband Rayleigh waves from correlations of the ambient seismic noise*. Geophys. Res. Lett., 31, L07614, doi: 10.1029/2004GL019419.

Shapiro N.M., Campillo M., Stehly L. and Ritzwoller M.H.; 2005: *High-resolution surface-wave tomography from ambient seismic noise*. Sci, 307, 1615-1618.

Takagi R. and Nishida K.; 2022: *Multimode dispersion measurement of surface waves extracted by multicomponent ambient noise cross-correlation funtions*. Geopys. J. Int., 231, 1196-1220, doi.org/10.1093/gji/ggac225.

Xiong X.S., Gao R., Li Q.S., Lu Z.W., Wang H.Y., Li W.H. and Guan Y.; 2009: *The Moho depth of South China revealed by seismic probing*. Acta. Geosci. Sin., 30, 774-786, in Chinese.

Yao H.J., Van Der Hilst R.D. and De Hoop M.V.; 2006; *Surface-wave array tomography in SE Tibet from ambient seismic noise and two-station analysis-I. Phase velocity maps.* Geophys. J. Int., 166, 732-744, doi: 10.1111/j.1365-246X.2006.03028.x.

Zhang Y.Y., Chen L., Ai Y.S., Jiang M.M., Xu W.W. and Shen Z.Y.; 2018: *Lithospheric structure of the south China block from S-receiver function*. Chin. J. Geophys., 61, 138-149, doi: 10.6038/cjg2018L0226, in Chinese.

Corresponding author: Peng Xue
College of Electrical and Electronic Engineering, Changchun University of Technology
Changchun 130021, China
Phone: +86 13596156955; e-mail: 910700148@qq.com